Applied Surface Science 609 (2023) 155245

Contents lists available at ScienceDirect

Applied Surface Science

journal homepage: www.elsevier.com/locate/apsusc

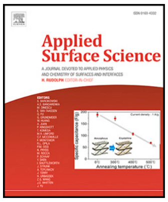

Full length article

Combinatorial aerosol deposition of bismuth–antimony thermoelectric coatings with tunable composition

Guanyu Song [a], Jesse M. Adamczyk [b], Eric S. Toberer [b], Christopher J. Hogan Jr. [a,*]

[a] *Department of Mechanical Engineering, University of Minnesota, Minneapolis, MN 55455, United States of America*
[b] *Department of Physics, Colorado School of Mines, Golden, CO 80401, United States of America*

ARTICLE INFO

Keywords:
Aerosol deposition
Thermoelectric coatings
In-situ alloying
Impact-driven melting
Molecular dynamics simulation
Formation mechanism

ABSTRACT

Aerosol deposition (AD) is commonly employed as a material processing step to generate coatings on substrates. In AD, aerosolized powders are passed through a nozzle and impacted at supersonic speeds onto the substrate. Plastic deformation of particles upon impact yields coatings with near bulk density. One key, unexploited advantage of aerosol processing is the ability to homogeneously mix disparate materials in the gas phase without concern over chemical compatibility or separation. Here, by using a custom-made voice-coil hopper injection (VHI) system for tunable injection of elemental powders, we demonstrate that AD can be applied directly in materials synthesis, depositing elemental precursor powders into homogeneous, dense coatings at adjustable atomic ratios. We examine the potential of combinatorial AD within the context of binary bismuth–antimony thermoelectric coating synthesis, adjusting the bismuth–antimony atomic ratio from 0.88:0.12, 0.75:0.25, to 0.5:0.5 and demonstrating that strongly adhered bismuth–antimony coatings can be produced via AD. Post-annealing is shown to yield solid bismuth–antimony solutions with thermoelectric properties approaching coatings produced by AD of pre-made, bismuth–antimony powders. Experiments are supplemented by molecular dynamics simulations of Bi and Sb nanoparticle sequential deposition, which reveal that the coating consolidation proceeds by plastic deformation and fracture of particles upon deposition.

1. Introduction

Versatile materials processing techniques, which can be used not only in materials manufacturing but also as a means for rapid synthesis during materials discovery, are highly desirable. For example, thermoelectric (TE) materials, which are typically binary, ternary, or quaternary compounds with additional dopants, are widely used in energy conversion applications because they can directly transform thermal energy into electrical energy [1]. There is interest in developing techniques to produce TE coatings with a variety of form factors (geometries) for a variety of applications, such as micro-TE generators [2] and micro-TE coolers [3]. There is also interest in developing accelerated high-throughput approaches to TE materials-discovery [4] as even for binary compounds, phase diagram mapping can require time-consuming solid-state synthesis methods. This could better be accomplished by automatically producing samples of systematically varied composition. Conventional TE coating deposition methods, such as electrophoretic deposition [5,6] and sputtering deposition [7,8], are also restricted by low growth rate as well as high production costs, and usually make coatings with high porosity, which adversely affects coating performance. They are further limited by the ability to easily tune coating chemistry as a means to probe the thermoelectric properties of different alloys.

A potentially more tractable route to producing TE coatings with the prescribed form factor and the ability to tune chemistry for TE materials discovery is aerosol deposition (AD) [9]. AD, also known as vacuum cold spray, is a solid-state particle deposition method wherein the particles, typically dispersed into an aerosol at atmospheric pressure, are accelerated to supersonic speeds through a converging or converging-diverging nozzle at near-vacuum conditions downstream. Particles then inertially impact onto target substrates beneath the nozzle, and with the nozzle rastered the coating form factor and thickness can be controlled. Importantly, particles with specific kinetic energies [10] falling into a narrow band [11–13] experience plastic deformation upon impact. When tuned properly, aerosol deposited particles are consolidated into near bulk density coatings with strong adhesion to the substrates; too low an impact velocity typically yields porous, weakly adhered coatings, and too high a velocity leads to substrate erosion [10].

A large number of proof-of-concept studies using AD to successfully print wide range of coating types onto different types of substrates have been carried out in the past several decades [14–16]. Most of

---

[*] Corresponding author.
E-mail address: hogan108@umn.edu (C.J. Hogan Jr.).

https://doi.org/10.1016/j.apsusc.2022.155245
Received 16 July 2022; Received in revised form 6 October 2022; Accepted 7 October 2022
Available online 13 October 2022

these studies are carried out with a single particulate precursor type, and without any chemical modification on precursor powder, e.g. $\alpha-Al_2O_3$ coatings onto polycarbonate substrate [17], Ag coatings onto alumina substrate [18], YSZ coatings onto aluminum substrate [12], TiO_2 coatings onto glass [19,20], and PMN-10PT thick films onto stainless steel [21]. However, single precursor powder use with AD does not fully exploit one of the key advantages of aerosol materials processing. In an aerosol, particles do not chemically interact with one another (such dispersions are dilute, and collision events are minimal during system transport time scales). Therefore, provided different particle types can be dispersed into an aerosol at controlled rates, mixing of nearly any combination of precursor materials is possible. In this instance, AD should yield a well-mixed deposit of all precursor powder particles, and because of the elevated kinetic energies during particle impact, AD may yield partial alloying as part of the impact process (in selected circumstances). Post-deposition annealing can be used to further alloy the materials together.

The use of multiple precursor particles with controlled relative injection rates would enable the use of AD towards materials discovery and coating production without the need for a priori synthesis of the coating (i.e., simpler element feedstock powders could be employed). However, to our knowledge, an AD implementation along these lines has not been experimentally realized. It appears the main reason for this is that controlled aerosolization of multiple solid powders simultaneously is difficult with commonly employed powder injection approaches; with a single precursor controlled injection is less of an issue as the rastering rate can be adjusted to compensate for the injection rate. Recently, Sinclair et al. [22] demonstrated that voice coils could be implemented in powder injection systems (though not for aerosols) to control mass flow rates of particles for applications in additive manufacturing. Here, we extend upon this approach to develop and apply a voice-coil hopper injection (VHI) system to disperse multiple powder feedstocks into an aerosol, enabling in-parallel deposition of multiple feedstocks. Given the noted importance of TE materials, and the need to develop coating and materials discovery processes for TE materials, we examine the performance of VHI-system facilitated AD in produced bismuth–antimony (bismuth–antimony) alloyed coatings. Bismuth–antimony alloys particularly have demonstrated strong thermoelectric performance at cryogenic temperatures and are one of the best TE materials at room temperature [23].

In the subsequent sections, we experimentally demonstrate the application of a VHI system towards the controlled injection of Bi and Sb elemental powders and the successful production of bismuth–antimony alloys through in-parallel AD with post-annealing. Furthermore, similar to prior simulation efforts [24], to provide greater insight into the in-parallel AD of multiple powder feedstocks, we utilize molecular dynamics (MD) simulations of Bi and Sb nanoparticle impacts onto a substrate and one another. Such simulations enable insight into the thermal and mechanical evolution of particles and the coating consolidation process [25–27]. Combined, the presented experimental studies and MD simulations demonstrate successful tuning of the bismuth–antimony coating composition, alloying post-deposition, and reveal the mechanism of coating formation via deformation, melting, and satellite particle-ejection, with successive deposition leading to densification.

2. Materials and methods

2.1. Precursor synthesis

For the parallel deposition of bismuth (Bi)–antimony (Sb) coatings, Bi (99.5%, Sky Spring) and Sb (99%, Aldrich) powders were applied and compared to pre-alloyed bismuth–antimony deposition. Bi (99.999%, Alfa Aesar) and Sb (99.999%, Alfa Aesar) pellets were used as the starting materials to prepare alloyed bismuth–antimony alloyed powder; their atomic ratio was adjusted to yield $Bi_{0.88}Sb_{0.12}$. Bi and Sb pellets were sealed and melted in a quartz ampoule under vacuum to produce alloys. After melting and resolidification, solid ingots of bismuth–antimony were annealed at 200 °C for 12 h to ensure compositional homogeneity throughout the mixed precursor compound. Annealed bismuth–antimony was then transferred into a stainless-steel milling container and sealed under an argon atmosphere (glove box). The milling process for the solid mixture was carried out with a high-energy ball milling machine (SPEX, SPEX SamplePrep) in isopropanol with yttria-stabilized zirconia (YSZ) milling balls for 2 h.

2.2. Voice coil aerosolization & coating deposition

Fig. 1 depicts the experimental system used in coating production, including a schematic diagram (Fig. 1a), the performance of the voice coil (H2 W Technologies)-hopper injection (VHI) system (Fig. 1b). Traditionally used in short stroke closed-loop servo applications, voice coil operating frequencies and amplitudes can be varied with a function generator, and in the VHI system, this leads to controlled, high-frequency vertical oscillations of the hopper and, consequently, the discharge of powder particles from the hopper at an adjustable-rate [22]. The VHI system can be used to uniformly dispense precursor powders across a range of powder materials, which is evidenced in Fig. 1b. In Fig. 1b, we plot the mass dispensed as a function of time (measured via a mass balance), for Bi, Sb, and Te micropowders, with the latter also shown to demonstrate applicability to additional materials. The discharge rate is observed to be extremely constant (highly linear plots) for all powders over one minute. At the same time, the discharge rate varies with particle composition and nozzle outlet diameter, alongside vibration frequency; hence the VHI system needs to be calibrated for each powder utilized.

Prior to coating deposition, the particle size distribution of the precursors was determined using an aerodynamic particle sizer (APS; TSI Inc, model 3330) and via scanning electron microscope images. APS measurements were made by sampling particles ejected from the VHI system and directed into the APS using dry air. Similar approaches for determining the size distribution of variable powders were reported in previous studies [28,29].

The deposition experiments performed were divided into in-series aerosol deposition and in-parallel aerosol deposition. For in-series AD (mixing followed by AD), alloyed $Bi_{0.88}Sb_{0.12}$ powder was used as aerosol precursor. For in-parallel AD (mixing during AD), Bi and Sb powder were dispensed by two VHI systems; the desired bismuth–antimony ratio in the aerosol precursor was obtained by tuning the frequency, the amplitude of the voice-coil-based powder dispenser and relative flow rate of compressed gas passed through powder dispenser nozzles. For both types of experiments, the system depicted schematically in Fig. 1a was utilized. With the voice coil or voice coils set to target frequencies, a total of 10 slm (standard liters per minute) of N_2 passed through the VHI nozzle outlets (with flow rates weighted by the target bismuth–antimony ratio in parallel experiments). An additional 5 slm of N_2 was added to further dilute precursor aerosol, yielding a particle flow at pressure 545 torr. The furnace in Fig. 1 was an optional component to heat the gas prior to expansion in the nozzle, but it was not employed in the current study. This flow was then sent to a converging-diverging slit nozzle impaction system, whose operation and dimensions are described in detail in Li et al. [11], Ghosh et al. [13], and Adamczyk et al. [30]. The slit nozzle has a throat width of 0.2 mm, and in it, particles were accelerated to supersonic speeds, entering a chamber at a pressure of 10 torr. Although the upstream operating pressure utilized in the present study is slightly lower than the atmospheric pressure operation used previously, prior simulations [11,12] suggest that ceramic particles in the 200 nm–2 μm diameter range achieve impact velocities in the 400–520 $m\ s^{-1}$ range, with the velocity decreasing with increasing particle diameter beyond 2 μm in diameter. The deposition velocity was therefore estimated to be hundreds of meters per second for the experiments reported here. 6.7 millimeters below the nozzle, 6 quartz 1 cm × 1 cm substrates

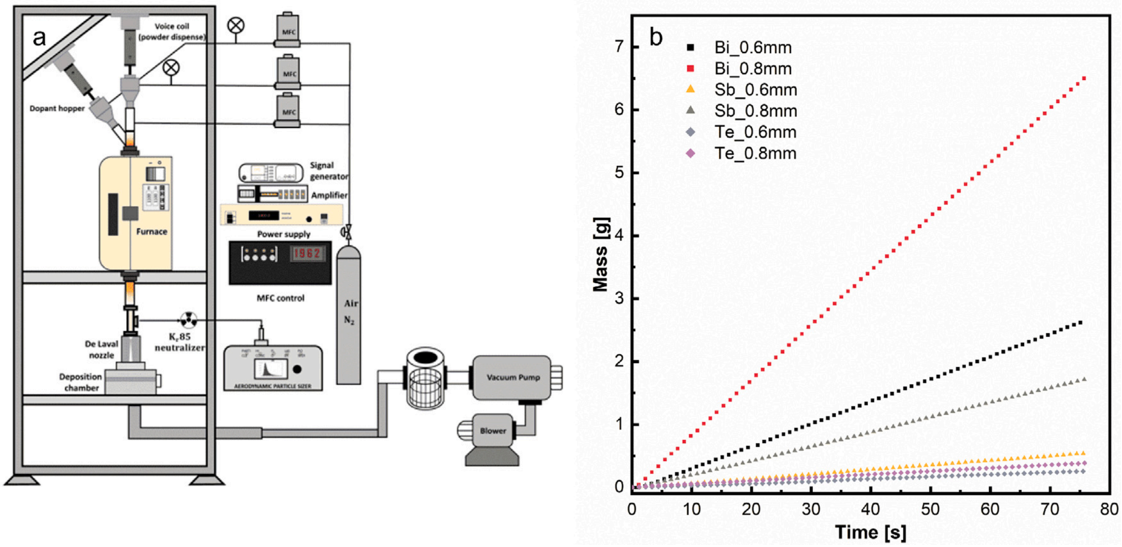

Fig. 1. Experimental setup **(a)** and powder mass as a function of time **(b)**.

were placed in a substrate holder. The holder was linearly translated at a speed of 1.06 mm s^{-1} perpendicular to the particle-laden flow, impinging upon the substrates. Simulations also indicate that under these conditions, Bi and Sb particles in size range aerosolized should impact the substrate with 100% efficiency, and while they may not adhere with perfect efficiency, this should facilitate coating formation. The main concern in coating experiments is, therefore, not ensuring particle impact with the substrate but instead ensuring consolidation of material upon impact. In total, we produced coatings varying the deposition time from 1 min to 10 min for pure Bi, $Bi_{0.88}Sb_{0.12}$, $Bi_{0.75}Sb_{0.25}$, and $Bi_{0.50}Sb_{0.50}$ with parallel AD. We only produced $Bi_{0.88}Sb_{0.12}$ with in series AD. The majority of as-deposited samples were then annealed at 200 °C for 1 h in argon gas.

2.3. *Material characterization*

X-ray diffraction (XRD) measurements were performed to characterize the crystal structure and phase for the precursor powders (Bi, Sb, and alloyed bismuth–antimony) and also for both annealed and un-annealed, deposited coatings on quartz substrates. The XRD spectra were acquired with a D8 Discover diffractometer (Bruker, Billerica, MA) using a Co radiation source (CoKα, $\lambda = 1.78897$ Å). XRD patterns for powder and coatings samples were collected for 2θ angle in the 20–95° range, with a step size of 0.01°. LaB_6 was used as an internal standard to account for instrumental peak broadening when inferring crystal sizes. MDI JADE software was used to identify phases and estimate crystallite sizes from diffraction peaks using the Scherrer equation. TOPAS V7 Academic was used to perform Rietveld refinement and obtain the elastic strain.

The coating surface morphologies, microstructures, and porosities were examined using a scanning electron microscope (SEM, SU8230) equipped with an energy-dispersive X-ray spectrometer (EDS). SEM measurements were collected with an acceleration voltage of 20 kV and a working distance range from 5 mm to 15 mm. As noted above, the size distribution of precursor powder was obtained by an aerodynamic particle sizer (APS); APS measurements were verified by manual size measurements with SEM images of more than 1000 particles. The elemental distribution and composition of as-deposited and post-annealed coatings were determined with EDS measurements. EDS spectra were acquired from 0 to 20 keV and analyzed using the Pathfinder software package (Thermo Scientific).

2.4. *Thermoelectric transport property measurement*

The room temperature Seebeck coefficients of the as-deposited and post-annealed coatings were measured in a custom apparatus, in which an 8–10 K temperature gradient was made laterally across each sample while the voltage drop across the sample was measured. Resistivity measurements were also made with a custom setup with a Van der Pauw four-point geometry. The pin spring contacts were positioned at the corners of each coating sample to measure resistivity. Finally, the carrier concentrations and mobilities of each coating were measured by the same apparatus in the same configuration but done in a magnetic field.

2.5. *Large-scale atomistic simulation*

To complement experiments and further investigate Bi and Sb particle mechanical and thermal responses during the coating consolidation process, we performed a series of large-scale molecular dynamics (MD) simulations with LAMMPS (Large-scale Atomic/Molecular Massively Parallel Simulator) [31] via the Minnesota Supercomputing Institute (MSI). Throughout the simulations, a two-body Morse potential form was used to represent the short-range interatomic interaction for the system. The potential parameters for bismuth–bismuth, antimony–antimony, and bismuth–antimony were adopted from previous studies wherein these potentials were derived from density functional theory [32,33]. In simulations, we considered two deposition scenarios. First, a spherical single-crystal Bi nanoparticle deposited at velocities of 500 m s^{-1} and 600 m s^{-1} on a Bi substrate. Second, two Bi nanoparticles at 500 m s^{-1} were impacted on a Bi substrate next to one another, and after this first impact event, a subsequent Sb nanoparticle with 500 m s^{-1} incident velocity was deposited upon the previously-deposited Bi particles. A Bi substrate was used in both scenarios with dimensions of $202\ \text{nm} \times 23.5\ \text{nm} \times 202\ \text{nm}$ (41,400,000 atoms). In lieu of simulating quartz as the substrate material, we simulated bismuth as the substrate material because we are interested in the coating growth process wherein depositing particles collide with previously deposited and consolidated bismuth and antimony. A 100 nm (14,877,066 atoms) diameter Bi particle was used in the first scenario, and two 65 nm diameter Bi particles and a 65 nm diameter Sb particle were used in the second scenario. The substrate and particle used in simulations were built from their corresponding unit cells. The substrate was divided into three different layers through the simulation: a Newtonian layer with a 300 K initial temperature and simulated as unthermostatted

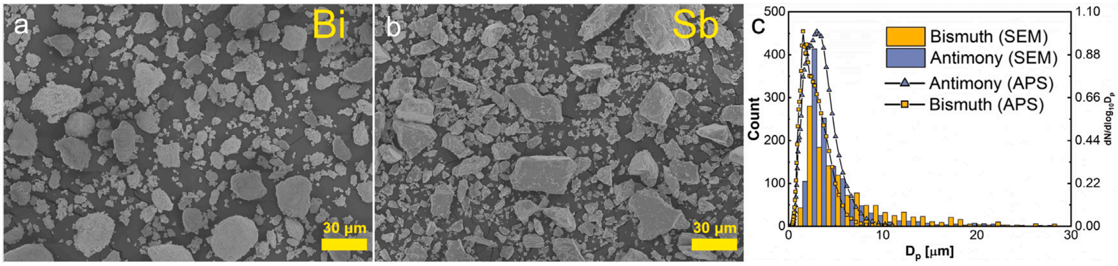

Fig. 2. Morphology of atomized bismuth powder **(a)**, antimony powder **(b)**, and size distribution derived from SEM micrographs and aerodynamic particle sizer **(c)**.

during deposition, a thermal layer (thermostat layer) that is simulated in an NVT (constant temperature) ensemble at 300 K to maintain room temperature, and an immobile layer. Prior to the impact event, the particle was placed 20 Å above the substrate, and both the thermal layer and Newtonian layer in the substrate, as well as the nanoparticle, were simulated in an NVT ensemble at 300 K via a Nose–Hoover thermostat for 250 ps. The time step used through the simulation was 0.5 fs. NVE relaxation was applied for another 100 ps ahead of the impact event to further thermalize the system. The microstructure and final morphology of the particles were visualized with the OVITO software package [34]. We specifically examine local and global particle temperature distributions throughout the deposition process, which were calculated following the approaches described in Song et al. [25]

3. Results & discussion

3.1. Voice coil-hopper injection-deposited coatings

The primary goal of the current study is the demonstration of tunable elemental ratios and spatially uniform elemental distributions in the parallel deposition of Bi and Sb, with the secondary goal of understanding the influence of post-processing (annealing) on coating crystallinity, using simulation to provide insight into coating consolidation at the nanoscale, and quantifying coating thermoelectric properties. The size distribution of Bi and Sb precursor powders determined from SEM micrographs are compared to the size distribution derived by using an aerodynamic particle sizer. The typical morphology of precursor powder particles, as observed via SEM, and size distribution results are shown in Fig. 2. Qualitatively, we find that Bi particles are more spherical than the Sb particles. Size distributions for both particle types are based upon projected area equivalent diameters in SEM, which are not equivalent to diameters from aerodynamic measurements (defined as the equivalent diameter in terms of mass-to-drag ratio). Nonetheless, the size distributions inferred from SEM images and aerodynamically are in excellent agreement with one another, yielding geometric mean diameters of 1.94 μm and 2.38 μm for bismuth and antimony powders, respectively. The good agreement between the two measurement approaches demonstrates that powders were dispersed into an aerosol relatively unagglomerated, and we conclude that the VHI system enables the successful aerosolization of micrometer-scale powders.

The XRD patterns of the precursor powders are displayed in Fig. 3a, both for the separate Bi and Sb powders, as well as pre-alloyed powder. The diffraction peaks in the Bi and Sb precursor powders match the reference peaks (Bi: PDF 98-001-5992, Sb: PDF 98-001-5986) with a rhombohedral structure, and we did not observe peaks corresponding to oxidized phases in the precursor. The strongest diffraction peaks (012) for Bi and Sb precursor powders are at 31.65° and 33.4° (2θ), respectively. For the alloyed $Bi_{0.88}Sb_{0.12}$ precursor powder, we observed peaks were shifted to higher (2θ) angles in the comparison to the reference peaks; for example, its Bi (012) reflection was shifted to 31.85°. There is complete solid solubility in the bismuth–antimony system, and thus increasing the concentration of Sb shifts the (012) reflection to larger values [35,36]. Due to the presence of Sb in the alloyed precursor powder, there was also a low-intensity characteristic peak at 33.38°.

Fig. 3b displays the XRD pattern for the as-deposited Bi and bismuth–antimony coatings, with the VHI and aerosol deposition systems operated as described in the methods section. Notably, in comparison to the precursor powder, the as-deposited coatings have broader peaks. For the Bi precursor powder and as-deposited coatings, we infer crystal sizes 136 nm and 74 nm, respectively. Peak broadening is attributable to a loss of crystallinity and the generation of micro-strain, commonly observed during AD processes for both metal and ceramic particles [37–39]. In addition, the thermal expansion anisotropy (TEA) can also lead to residual stress and crystal fracture resulting in peak broadening, which has been investigated in previous research [40,41]. The enlarged view of the (012) reflection of as-deposited coatings shown in Fig. 3c also demonstrates a noticeable peak shift in both the in-parallel-deposited and in-series-deposited bismuth–antimony binary coatings, especially in $Bi_{0.88}Sb_{0.12}$ coatings. The peak shift in the in-series-deposited material is not surprising, given that it is pre-alloyed powder. However, observation of peak shift in the parallel-deposited coating is suggestive of some degree of alloying during the deposition process, where the Sb atoms replace the Bi atoms in the Bi lattice. Though less likely, other possibilities include two unresolved peaks in the in-parallel deposited spectrum. We also find evidence that deposition leads to some degree of oxidation, even in an environment kept at low levels of O_2, as an oxidized bismuth phase was found in Bi and bismuth–antimony coatings (Fig. 3d). While the bismuth oxide peaks detected are low in signal intensity, we note that such peaks were not discernable in the precursor powders. We attribute the formation of an oxidized phase to the transient but extremely high temperature of Bi particles during deposition processes. As shown in prior simulations during aerosol deposition, translational-to-thermal energy conversion in particles leads to transient particle heating before energy is entirely dissipated into the substrate or existing coating [42]. This is likely particularly important for Bi, which has a low melting temperature and may enter a semi-molten or molten state during the coating process. We provide further evidence for this, along with evidence for incorporation of Sb into the Bi crystal structure during deposition, with MD simulations subsequently.

We utilized a scanning electron microscope to investigate the microstructure and morphology of the as-deposited coatings. Without rastering the substrates beneath the nozzle, a bismuth–antimony line was deposited in-parallel, and is shown in Fig. 4a (left). We examine this coating first as a such frustum, pyramid-shaped coatings are commonly observed in lines deposited by gas dynamic cold spray and related approaches [18,43,44], presumably due to aerodynamic focusing of particles in nozzle systems, which is a strong function of particle size [11]. The success of bismuth–antimony line deposition indicates that the property differences and size distribution deviation in Bi and Sb particles did not hinder coating growth. However, the crack observed in the bismuth–antimony pyramid frustum is likely due to the internal stress accumulated within the deposit, which is of concern and needs to be examined in preparing more extensive

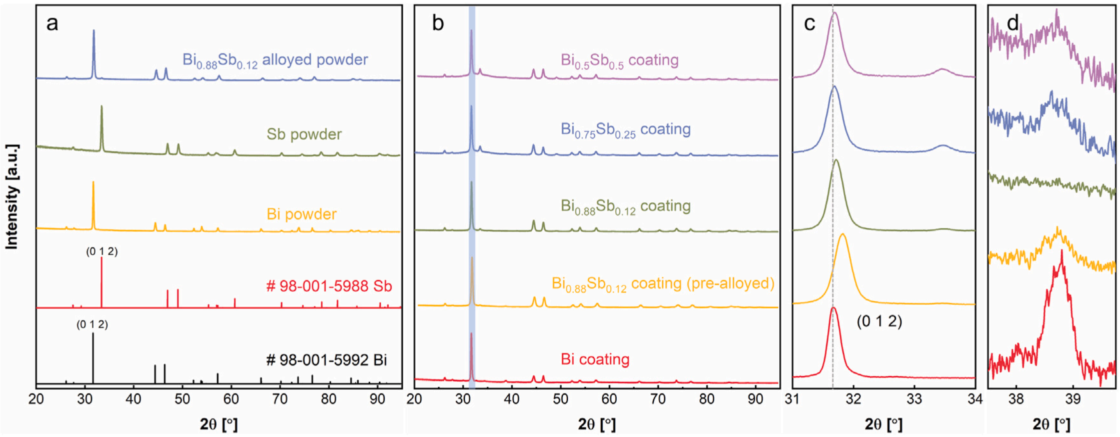

Fig. 3. XRD pattern for bismuth, antimony, and alloyed $Bi_{0.88}Sb_{0.12}$ powder **(a)**, as-deposited coatings with variable bismuth–antimony ratio **(b)** an enlarged view of (012) reflection **(c)**, bismuth oxide phase found in as-deposited films **(d)**.

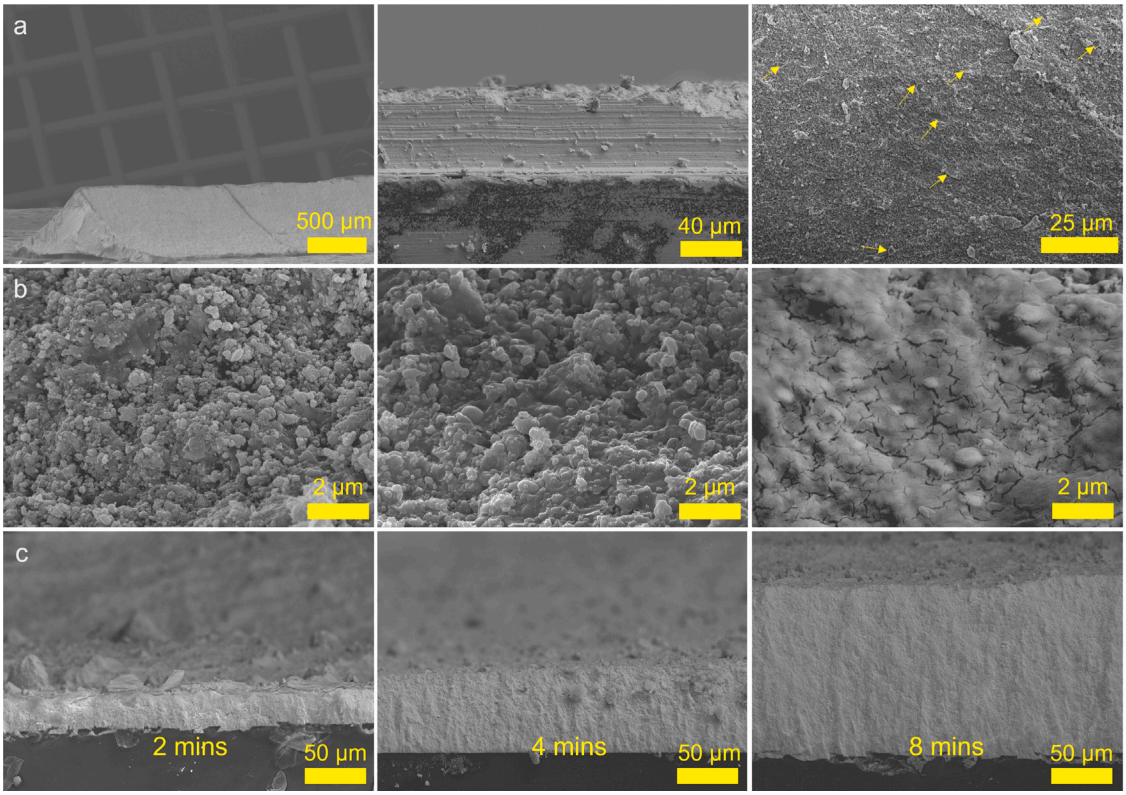

Fig. 4. Line-deposited $Bi_{0.88}Sb_{0.12}$ pyramid (left), cross-section view SEM image for as-deposited $Bi_{0.88}Sb_{0.12}$ coating (middle), surface morphology of as-deposited coating with yellow arrows pointing to splats (right) **(a)**. Zoom-in view of particle splats and satellites (left and middle) and post-annealed coating surface morphology (right) **(b)**. Side view SEM image for as-deposited $Bi_{0.88}Sb_{0.12}$ coatings with increasing deposition period **(c)**.

area coatings. The cross-section and the surface morphology of as-deposited, in-parallel coatings are presented in Fig. 4a, as the center and rightmost images, respectively. As evidenced by observed resultant surface morphology, the VHI deposited coatings have relatively higher roughnesses in comparison to the coatings manufactured by high-temperature processes, indicating that during deposition, particles do not completely coalesce with the pre-existing coating (i.e., while deposition facilitates deformation and changes at the atomic level, as evidenced in XRD, SEM images show coatings retain particle features at the top, most recently deposited level). There are also clear regions containing particle “splats”, commonly observed in thermal plasma deposition processes wherein particles are molten before colliding with the substrate [45]. We mark such regions with yellow arrows in Fig. 4a (right), and these areas are observed at higher magnification in Fig. 4b (left and middle). Upon viewing at higher magnification, we observe that these regions contain submicrometer particles not observed in the original size distribution. Presumably, these satellite particles are formed during the deposition of semi-molten material. We later confirm this through atomistic simulations.

To gain insight into the coating solidity within the depth of the coating, we cut through the as-deposited coating samples and obtained side-view SEM images. As displayed in Fig. 4a (middle), the as-deposited bismuth–antimony coatings were highly dense, and only a few cracks or pores were found in the coatings. While coating surfaces are rough, the resultant dense structure in the as-deposited coatings can be attributed to a “hammering” effect characteristic of

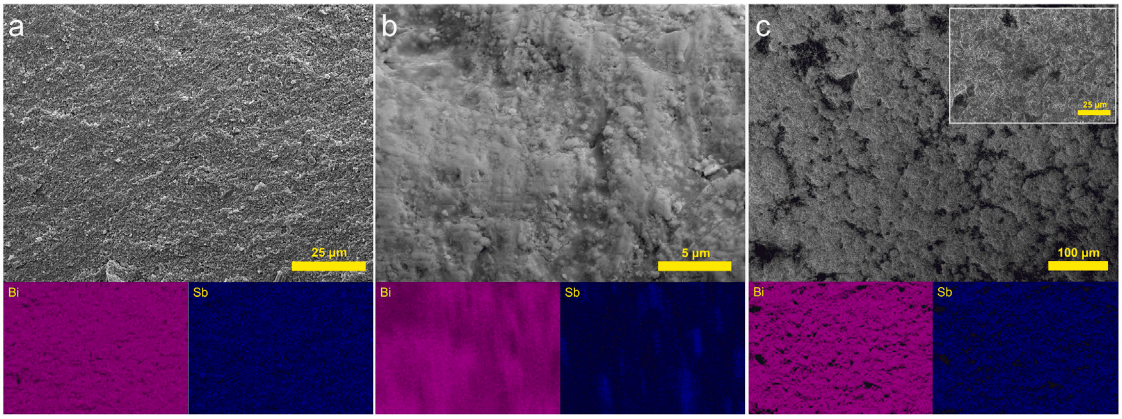

Fig. 5. Surface **(a)**, side-view **(b)** SEM images and EDS chemical mappings for the as-deposited $Bi_{0.88}Sb_{0.12}$ coating, and for a post-annealed $Bi_{0.88}Sb_{0.12}$ coating, with a zoomed-in inset **(c)**.

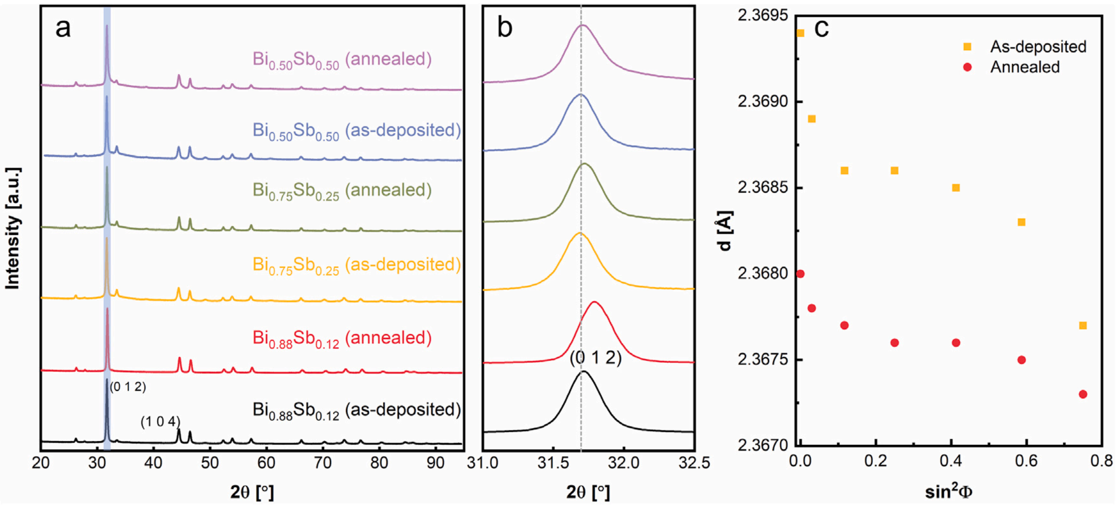

Fig. 6. XRD pattern for as-deposited and post-annealed coatings with variable bismuth–antimony ratios **(a)**, enlarged view of (012) reflection **(b)**, and interplanar distance as a function of $\sin^2(\phi)$ for as-deposited and annealed $Bi_{0.88}Sb_{0.12}$ coating **(c)**.

AD, where multiple particle impacts on top of deposited material lead to densification [10,46]. Fig. 4a cross-sectional SEM image also enables examination of the adhesion between the substrate and coating; coatings appear well-adhered to substrates, but without substrate penetration or damage, observed at higher velocities and harder depositing materials. Fig. 4c displays a sequence of side-view bismuth–antimony coatings (without cutting into the coating, hence surface roughness is evident) with an increased deposition period. Continuously increasing thickness indicates tunable coating thickness, alongside tunable elemental composition, is possible by adjusting deposition time.

A surface SEM image and EDS mapping for parallel-deposited $Bi_{0.88}Sb_{0.12}$ coating are displayed presented in Fig. 5. EDS measurements were taken at multiple positions on the surface of the coatings to study the homogeneity of elemental ratio in the as-deposited coatings. We observe that both Bi and Sb elemental distributions are relatively homogeneous throughout the sample surface at the micro-scale. Side-view EDS mapping results also demonstrate that Bi and Sb particles were mixed vertical as coating growth occurred. Homogeneity is maintained upon annealing parallel-deposited coatings (Fig. 5c), although the inset of Fig. 5c shows there were some peculiar whiskers that developed on the surface of post-annealed coatings with lengths of few µm.

Fig. 6a displays the XRD pattern for a series of as-deposited and annealed coatings with a zoom-in of the Bi (012) peak in Fig. 6b. While annealing does lead to shifts in the (012) peak location, interestingly, we observe larger peak shifts with lower Sb concentrations. At the same time, after the annealing process, the Sb (012) reflection disappeared in $Bi_{0.88}Sb_{0.12}$ coatings but still can be observed with a diminished intensity for higher Sb-doped coatings. These combined findings suggest that the alloying was only complete in $Bi_{0.88}Sb_{0.12}$ coatings and longer post-annealing process is required to make alloying complete in $Bi_{0.75}Sb_{0.25}$ and $Bi_{0.5}Sb_{0.5}$ coatings.

We do not observe substantial changes in inferred crystal sizes through annealing. To further investigate the effects of post-annealing on the coatings, we performed tilt-angle-dependent XRD measurements, also known as the $\sin^2(\phi)$ method, for the (104) reflection at tilting angles (ϕ) from 0 to 60°. The inferred interplanar spacing as a function of $\sin^2(\phi)$ is presented in Fig. 6c. For the as-deposited coatings, we find that the interplanar spacing reduces with an increase in tilt angle, accordingly suggesting there are compressive in-plane residual stresses developed during the AD process. While compressive in-plane stress remains in annealed coatings, where the interplanar spacing also reduces with tilt angle, we find a reduced magnitude of the sensitivity to tilt angle, suggesting annealing reduces residual stress. In addition to the compressive stress caused by deposition, there are likely additional stresses caused by the thermal mismatch with the alumina substrate and thermal expansion anisotropy. Calculation of thermal substrate mismatch stress requires significant assumptions of the temperature-dependent mechanical properties that cause an overestimation of the stresses. As such, the calculation of the elastic strain from Rietveld refinement should incorporate all strain effects yielding a single stress

Table 1
VHI operating parameters and bismuth–antimony elemental ratios found in the as-deposited coatings, extracted from EDS spectra.

	VHI frequency (Hz)		VHI amplitude (V)		Nozzle diameter (mm)		As-deposited bismuth–antimony ratio	Expected bismuth–antimony ratio
	Bi	Sb	Bi	Sb	Bi	Sb		
$Bi_{0.88}Sb_{0.12}$	600	520	3.5	1.2	0.8	0.5	11.59 ± 0.33	12.59
$Bi_{0.75}Sb_{0.25}$	520	650	3.0	3.5	0.8	0.6	5.37 ± 0.71	5.15
$Bi_{0.5}Sb_{0.5}$	500	680	3.0	4.0	0.8	0.8	2.24 ± 0.12	1.72

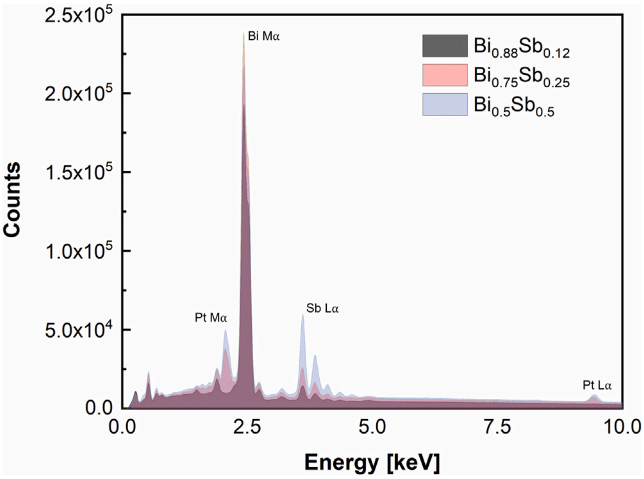

Fig. 7. EDS spectra for bismuth–antimony coatings with variable stoichiometries integrated over complete image areas.

value. Negligibly small stress values of ~0.01 MPa were refined for annealed Bi and $Bi_{0.75}Sb_{0.25}$ samples, respectively. We also observe that the interplanar distances for post-annealed coatings at all tilt angles are smaller than the as-deposited coatings; this suggests the annealing process improves the mixing of Bi and Sb elements, as more Bi atoms in the Bi lattice were replaced by Sb atoms, and the lattice slightly deformed, resulting in the overall Bragg angles shift to higher values. Such changes in peak position and broadening are likely driven by the changes in alloy chemistry rather than residual stresses.

The elemental ratios provided for coatings refer to that expected based upon aerosolization rates. EDS spectra for coatings are provided in Fig. 7 and confirm that as more Sb particles are aerosolized relative to Bi particles, the peaks for Sb elements have higher intensity. The EDS-extracted bismuth–antimony elemental ratios for $Bi_{0.88}Sb_{0.12}$, $Bi_{0.75}Sb_{0.25}$, and $Bi_{0.5}Sb_{0.5}$ are provided in Table 1 alongside the VHI system frequencies and amplitudes in operation, nozzle diameters employed, and expected elemental ratios for the target mass ratio. Overall, the bismuth–antimony ratio found in the as-deposited coatings is in reasonable agreement with targetted values. The elemental ratio in the $Bi_{0.5}Sb_{0.5}$ coatings has the largest deviation from the target, attributable to powder size distribution-dependent VHI system aerosolization rates and deposition rates in the system upstream of the nozzle. However, even accounting for this deviation, VHI experiments reveal that in-parallel deposited coatings with tunable composition can be produced, which are dense, tens of micrometers in thickness, and which can be annealed to produce alloys.

3.2. Atomistic simulation of coating consolidation

While demonstrative towards application, with few exceptions, experiments in AD often do not provide insight into the mechanism of coating formation and into the effect the high-speed impact process has on both particles and substrates mechanically. To better understand coating formation within the context of binary, in-parallel deposition towards alloyed coatings, we utilize atomistic simulations. There are several previous studies suggesting local melting occurs in the deformed particles during high-speed impacts [47–49], which may be essential to consider during in-parallel deposition. For example, recent studies of cold spray deposition of pre-made SnBi alloys reveal a high degree of particle melting occurs during the coating process [50].

Fig. 8a shows the global temperature evolution of a simulated 100 nm Bi nanoparticle with both 500 m s^{-1} and 600 m s^{-1} incident velocities during impact with Bi substrate. The insets depict the morphologies and local temperature distributions of Bi nanoparticles at the instance of its highest global temperature, marked by arrows in the main portion of the figure. Global temperature evolution results indicate that the maximum global temperatures developed in Bi nanoparticles impact at 500 m s^{-1} and 600 m s^{-1} are 1300 K and 980 K, respectively. Determined in prior MD simulations, the melting temperature of bismuth is near 558 K [51] (though for different potentials). We, therefore, clearly observe that the maximum global temperature in the bismuth nanoparticles is well beyond the melting temperature. The high temperature within the nanoparticle can also lead to plasticity within it during the deposition process, which is also reported in simulations of hydroxyapatite nanoparticle impact [52]. As particles exceed the melting temperature during deposition, they unsurprisingly undergo drastic amounts of plastic deformation during the deposition. While recent simulations suggest that melting is not necessary for successful AD of ceramics, it appears highly likely that melting upon impact facilitates coating consolidation for Bi and presumably for many elemental precursors of interest in binary thermoelectric compounds (e.g., SnTe, PbTe, Bi_2Te_3, etc.).

Common neighbor analysis (CNA) was employed to identify the local crystalline of atoms within the nanoparticle [34,53]. While not shown directly, we find that following deposition, the regions of the Bi nanoparticle in contact with the substrate are no longer crystalline (with the nanoparticle a single crystal initially). Also, at the end of simulations, we examined final particle morphologies (Fig. 8b), and similar to experiments, we observed particles had formed fractured splat-like deposits. We also find that a number of small clusters are emitted from the incident particle during the impact event and that the particle is no longer a single continuous particle. This, too, is consistent with the coating surface morphology we observed in surface SEM micrographs. Atomistic simulations hence demonstrate that experimentally observed coating morphologies result from melting, high deformation, and satellite particle ejection during the deposition for Bi. We remark, again, however, that these observations are not universal in AD, e.g., atomistic simulations of higher melting temperature ceramic materials do not yield similar extents of plastic deformation, fracture, and satellite particle formation [54].

While there are a considerable number of prior atomistic simulations of AD, to our knowledge, the majority of these efforts focus on the impact of a single particle and not the build-up of a coating through successive particle impact events. Fig. 9 displays the results of simulations of layer build-up during in-parallel AD where two Bi nanoparticles are first deposited next to one another in tandem, and an Sb nanoparticle is deposited in between (i.e., at the center of the domain) the neighboring Bi nanoparticles. As indicated by Fig. 9a, which is a global temperature versus time plot, the first two deposited Bi nanoparticles reach a maximum global temperature of more than 1300 K, again leading to deformation, melting, and satellite particle ejection. However, we do observe some differences from the single

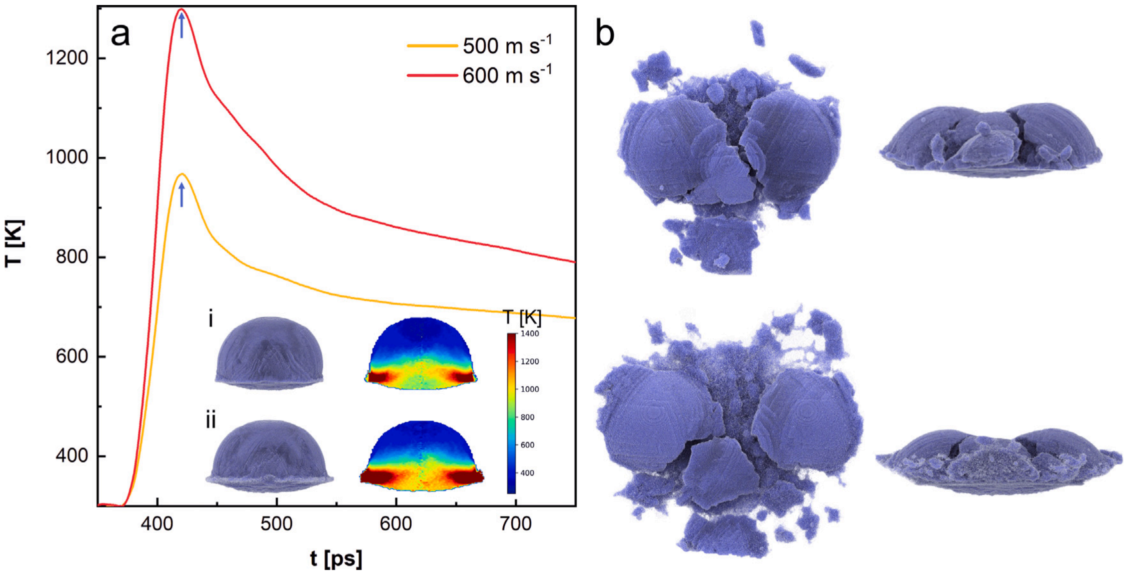

Fig. 8. 100 nm Bi nanoparticle global temperature evolution (with local temperature distributions at maximum global temperatures shown) **(a)** and the morphologies of Bi nanoparticle with 500 m s^{-1} and 600 m s^{-1} incident velocity at the end of simulations **(b)**.

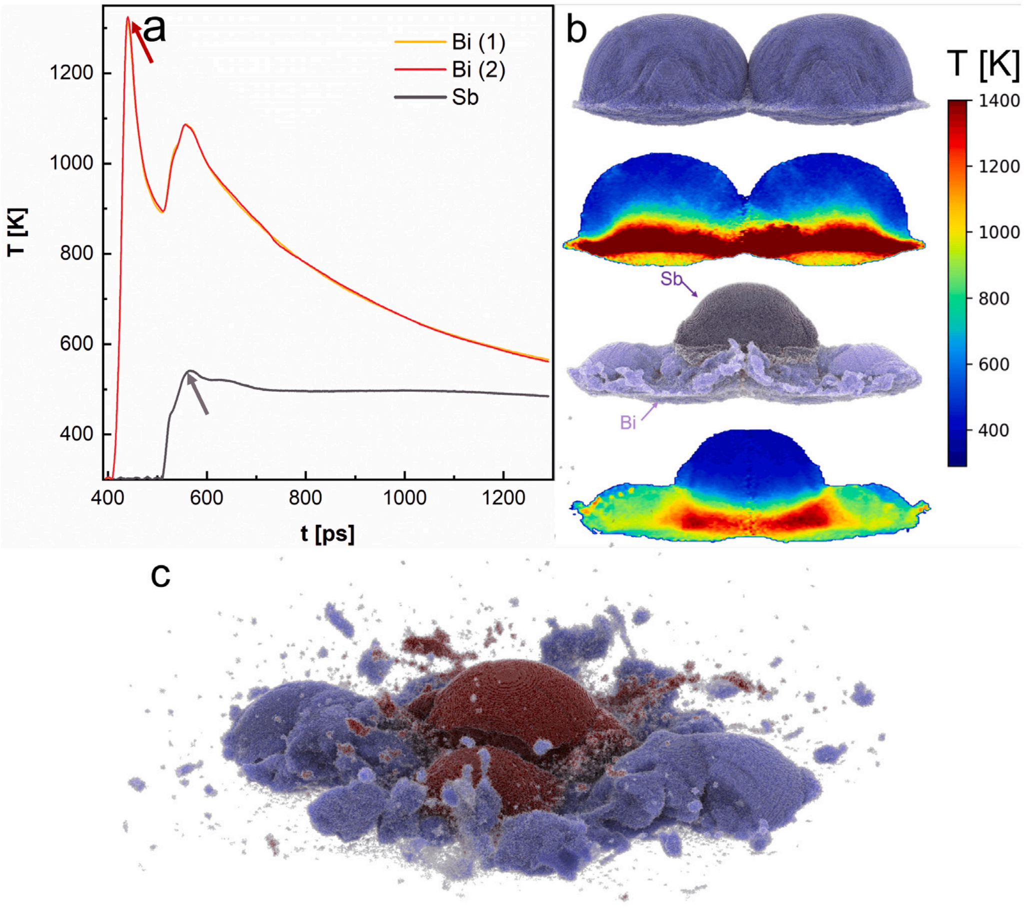

Fig. 9. The global temperature evolution of Bi and Sb nanoparticles during layer build-up **(a)**, the nanoparticle morphology and local temperature distribution at the instance of maximum global temperature for Bi and Sb **(b)**. The morphology of two deposited Bi nanoparticles and a central deposited Sb nanoparticle at the end of the simulation **(c)**.

nanoparticle deposition simulations; in Fig. 9b, we display the morphology and local temperature distributions for both Bi nanoparticles at the instance of maximum global temperature. For single Bi nanoparticle impact, the highest temperature regions are located in the particle radial periphery, with the reduced temperature at the particle center. However, the high-temperature zone extends across the entirety of both Bi nanoparticles deposited simultaneously. This extended high-temperature area within the nanoparticles can be attributed to the lateral interactions between two Bi nanoparticles during the impact event, as they partially coalesce with one another. Subsequently, when

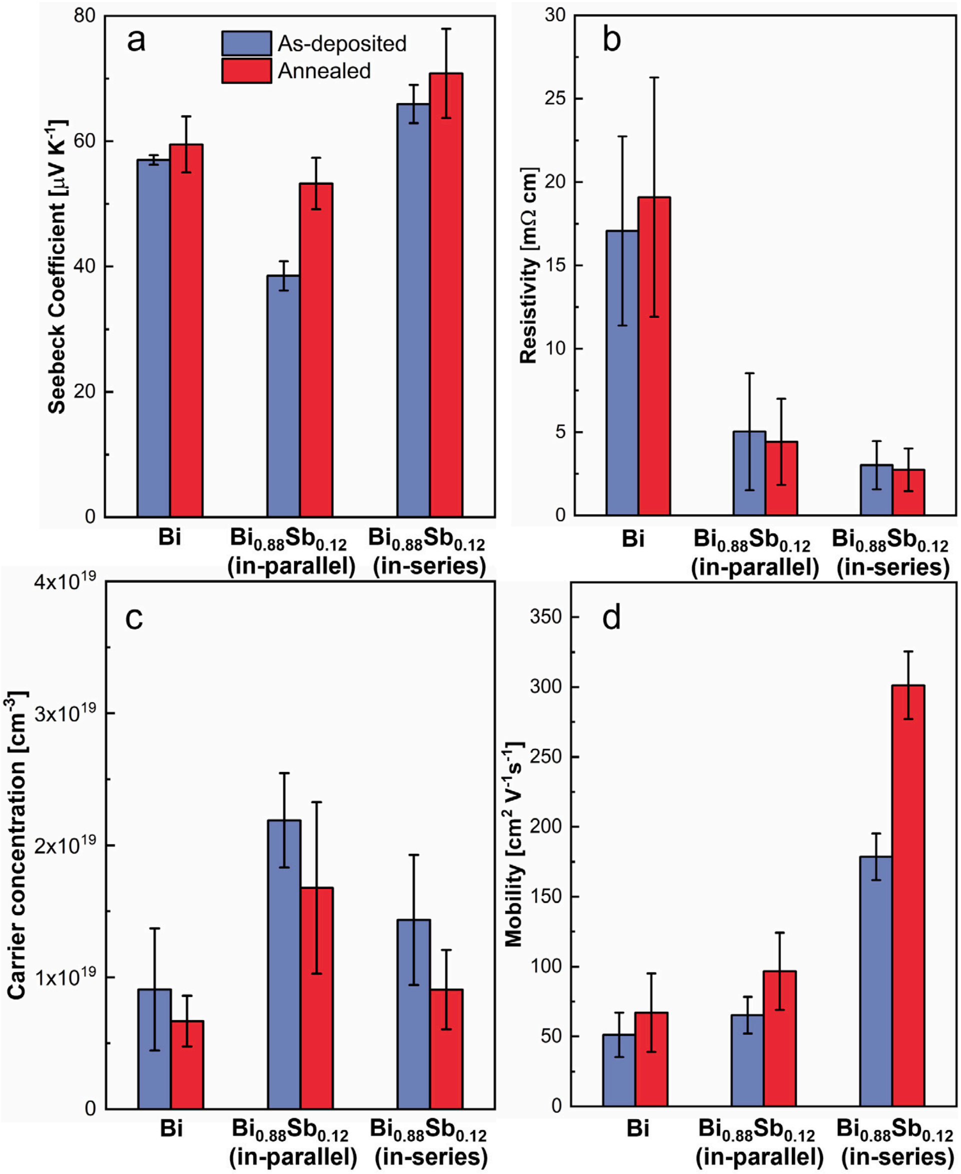

Fig. 10. Transport properties for bismuth coatings, in-parallel deposited $Bi_{0.88}Sb_{0.12}$, and $Bi_{0.88}Sb_{0.12}$ coatings deposited with alloyed powder: Seebeck coefficient **(a)**, resistivity **(b)**, carrier concentration **(c)**, and mobility **(d)**.

the Sb nanoparticle deposits, global temperature evolution and morphology results presented in Fig. 9a and 9b (top) indicates that the subsequent deposition event not only results in the second rise in Bi nanoparticle temperatures but also leads to additional deformation and coalesce of the Bi deposits with one another (i.e., we confirm that subsequent deposition leads to a hammering effect). Fig. 9b (bottom) additionally shows that the Sb nanoparticle heats up the previous Bi layer. At the end of the simulations, the Sb nanoparticle global temperature and the Bi nanoparticle global temperatures were still elevated, as time is required for the nanoparticles to dissipate all thermal energy to the substrate. While this suggests that the coating may have an elevated temperature during AD, we note that the time between Bi impact and Sb impact was only 50 ps in simulations, and realistically, the average time between particle collisions with the substrate is 10^{-1}–10^{2} ns (dependent on particle concentration in the system and the flow rate), and hence heat likely fully dissipates between collisions. Finally, we remark that although simulations can be used to provide insight into nanoparticle structural and thermal evolution during deposition, we do not simulate annealing, which would require longer simulation times than possible for the potentials applied and at temperatures employed in experiments. Annealing, of course, leads to additional changes at the atomic level, including new bonding (alloying) [55]

3.3. Thermoelectric properties

The thermoelectric properties of pure Bi coatings, pre-alloyed $Bi_{0.88}Sb_{0.12}$, and in-parallel deposited $Bi_{0.88}Sb_{0.12}$ were studied, both before and after annealing. Pure Bi was studied to provide a baseline material to compare the thermoelectric properties of in-parallel deposited and in-series deposited coatings. Results are summarized in Fig. 10. Bi and Sb are both semimetallic in their elemental forms [56], but Bi exhibits *n*-type behavior and Sb, *p*-type behavior. For both elemental materials, the origin of the majority carrier type (electrons or holes) stems from the position of the Fermi level relative to the respective band edge. For Bi, the Fermi level is deeper in the conduction band (*n*-type), while for Sb, the Fermi level lies in the valence band (*p*-type) [57]. The moderate Seebeck coefficient measured for Bi is in agreement with prior measurements [58]; however, the high resistivity and low mobility appear to be the result of the plastic deformation that occurs during the deposition process. All bismuth–antimony coatings were found to show *n*-type semiconducting behavior, consistent with the findings from previous reports [59,60]. The bismuth–antimony alloy forms a full solid solution with a unique band structure that changes as a function of composition. Both elemental Bi and Sb do not have a gap (semimetallic behavior); however, between 2.3–22 atomic percent Sb doped into Bi, the bismuth–antimony alloy band gap widens, and semiconducting behavior is observed [60,61]. Evidence of the widening gap is seen in Fig. 10a, where the pre-alloyed samples show the highest Seebeck coefficient in comparison to the Bi and in-parallel deposited samples. Pre-alloyed samples are disordered at the atomic scale through substitutional alloying. Unlike materials that partition into multiple phases, the bismuth–antimony alloy system forms a single phase where each atomic site contains either a Bi or Sb atom, depending on the relative concentrations of the elements. This substitutional alloy behavior widens the band gap, as evidenced by the higher Seebeck coefficient, lower carrier concentration, and higher mobility. In contrast, samples deposited from elemental Bi and Sb (unmixed) precursors lack the atomic scale disorder required to open the band gap. In-parallel deposition results in a mixture of discrete *n*-type Bi and *p*-type Sb grains that cause a reduced Seebeck coefficient as a result of the competing *n*- and *p*-type behavior. The competing effects can be overcome by annealing and homogenizing the in-parallel deposited films (Fig. 10a), improving the Seebeck coefficient and mobility. Therefore, while the deposition process introduces significant plastic deformation, consistent with XRD measurements, achieving atomic-scale chemical homogeneity of aerosol deposited films requires thermal treatment in order to drive mass transport and substitution within the coatings. At the same time, we find that in-parallel deposition of atomic precursors can be used to produce coatings of a target chemical composition, and with thermoelectric properties after annealing approaching in-series, pre-alloyed materials.

4. Conclusion

We developed an in-parallel AD process to produce bismuth-antimony thermoelectric coatings with tunable compositions. By combining a custom-developed VHI system with AD, we were able to control powder injection rates in AD, and we have successfully made $Bi_{0.88}Sb_{0.12}$, $Bi_{0.75}Sb_{0.25}$, and $Bi_{0.5}Sb_{0.5}$ coatings with elemental homogeneity. We demonstrate that instead of using AD only as a final processing step only to adjust the form factor, it can be applied as a step in materials synthesis. Materials characterization results for as-deposited coatings indicate that Bi and Sb elements were mixed in AD, and post-annealing performed on the as-deposited coatings can help to widen the band gap of the coatings, leading to improved thermoelectric properties.

Large-scale MD simulations were performed to supplement experiments, permitting observation of the binary coating consolidation process. Single-particle deposition simulation results indicate that the Bi nanoparticles during AD experience extreme plastic deformation with high strain rates, melting, fracture, and satellite particle ejection. Simulations of sequential deposition of Bi and Sb nanoparticles reveal that sequential deposition of particles onto pre-existing layers facilitates densification. Satellite particle ejection observed in MD simulations coincides with observations of such particles in SEM images.

CRediT authorship contribution statement

Guanyu Song: Conceptualization, Methodology, Validation, Formal analysis, Investigation, Data curation, Writing – original draft, Writing – review & editing, Visualization. **Jesse M. Adamczyk:** Conceptualization, Methodology, Validation, Formal analysis, Investigation, Writing – original draft, Writing – review & editing. **Eric S. Toberer:** Conceptualization, Methodology, Resources, Supervision, Project administration, Funding acquisition. **Christopher J. Hogan Jr.:** Conceptualization, Methodology, Resources, Writing – original draft, Writing – review & editing, Supervision, Project administration, Funding acquisition.

Declaration of competing interest

The authors declare that they have no known competing financial interests or personal relationships that could have appeared to influence the work reported in this paper.

Data availability

Data will be made available on request.

Acknowledgments

This work was supported by the ARPA-E, United States award DE-AR0001094. The authors acknowledge the Minnesota Supercomputing Institute (MSI) at the University of Minnesota for providing high-performance computational resources. Parts of this work were carried out in the Characterization Facility at the University of Minnesota, which receives partial support from the NSF through the MRSEC, United States (Award Number DMR-2011401) and the NNCI, United States (Award Number ECCS-2025124) programs.

References

[1] G. Jeffrey Snyder, Eric S. Toberer, Complex thermoelectric materials, Nature Mater. 7 (2) (2008) 105–114.

[2] Paul Fourmont, Luis Felipe Gerlein, Francois-Xavier Fortier, Sylvain G Cloutier, Riad Nechache, Highly efficient thermoelectric microgenerators using nearly room temperature pulsed laser deposition, ACS Appl. Mater. Interfaces 10 (12) (2018) 10194–10201.

[3] Simon Corbett, D Gautam, Swatchith Lal, Kenny Yu, Naveen Balla, Graeme Cunningham, Kafil M Razeeb, Ryan Enright, David McCloskey, Electrodeposited thin-film micro-thermoelectric coolers with extreme heat flux handling and microsecond time response, ACS Appl. Mater. Interfaces 13 (1) (2021) 1773–1782.

[4] Juan J de Pablo, Nicholas E Jackson, Michael A Webb, Long-Qing Chen, Joel E Moore, Dane Morgan, Ryan Jacobs, Tresa Pollock, Darrell G Schlom, Eric S Toberer, et al., New frontiers for the materials genome initiative, Npj Comput. Mater. 5 (1) (2019) 1–23.

[5] Tahereh Talebi, Reza Ghomashchi, Pejman Talemi, Sima Aminorroaya, Fabrication of n-type Bi2Te3 film using electrophoretic deposition for thermoelectric applications, Surf. Coat. Technol. 343 (2018) 127–130.

[6] Tahereh Talebi, Reza Ghomashchi, Pejman Talemi, Sima Aminorroaya, Thermoelectric performance of electrophoretically deposited p-type Bi2Te3 film, Appl. Surf. Sci. 477 (2019) 27–31.

[7] Xing Wang, Hongcai He, Ning Wang, Lei Miao, Effects of annealing temperature on thermoelectric properties of Bi2Te3 films prepared by co-sputtering, Appl. Surf. Sci. 276 (2013) 539–542.

[8] Masahiro Goto, Michiko Sasaki, Yibin Xu, Tianzhuo Zhan, Yukihiro Isoda, Yoshikazu Shinohara, Control of p-type and n-type thermoelectric properties of bismuth telluride thin films by combinatorial sputter coating technology, Appl. Surf. Sci. 407 (2017) 405–411.

[9] Jun Akedo, Maxim Lebedev, Microstructure and electrical properties of lead zirconate titanate (Pb (Zr52/Ti48) O3) thick films deposited by aerosol deposition method, Japan. J. Appl. Phys. 38 (9S) (1999) 5397.

[10] Dominik Hanft, Jörg Exner, Michael Schubert, Thomas Stöcker, Paul Fuierer, Ralf Moos, An overview of the aerosol deposition method: Process fundamentals and new trends in materials applications, J. Ceram. Sci. Technol. 6 (3) (2015) 147–182.

[11] Chenxi Li, Narendra Singh, Austin Andrews, Bernard A Olson, Thomas E Schwartzentruber, Christopher J Hogan Jr., Mass, momentum, and energy transfer in supersonic aerosol deposition processes, Int. J. Heat Mass Transfer 129 (2019) 1161–1171.

[12] Guanyu Song, Jesse Adamczyk, Yensil Park, Eric S Toberer, Christopher J Hogan Jr., Spray pyrolysis-aerosol deposition for the production of thick Yttria-stabilized Zirconia coatings, Adv. Eng. Mater (2021) 2100255.

[13] Souvik Ghosh, Xiaoshuang Chen, Chenxi Li, Bernard A Olson, Christopher J Hogan Jr., Fragmentation and film growth in supersonic nanoaggregate aerosol deposition, AIChE J. 66 (4) (2020) e16874.

[14] Neamul H Khansur, Udo Eckstein, Kevin Riess, Alexander Martin, Jakub Drnec, Ulrike Deisinger, Kyle G Webber, Synchrotron x-ray microdiffraction study of residual stresses in BaTiO3 films deposited at room temperature by aerosol deposition, Scr. Mater. 157 (2018) 86–89.

[15] Matej Sadl, Andrej Lebar, Josko Valentincic, Hana Ursic, Flexible energy-storage ceramic thick-film structures with high flexural fatigue endurance, ACS Appl. Energy Mater. (2022).

[16] Wai Kian Tan, Yuichi Shigeta, Atsushi Yokoi, Go Kawamura, Atsunori Matsuda, Hiroyuki Muto, Investigation of the anchor layer formation on different substrates and its feasibility for optical properties control by aerosol deposition, Appl. Surf. Sci. 483 (2019) 212–218.

[17] Jun Akedo, Aerosol deposition of ceramic thick films at room temperature: Densification mechanism of ceramic layers, J. Am. Ceram. Soc. 89 (6) (2006) 1834–1839.

[18] JJH McCallister, MD Gammage, JW Keto, MF Becker, D Kovar, Influence of agglomerate morphology on micro cold spray of Ag nanopowders, J. Aerosol Sci. 151 (2021) 105648.

[19] Jesse Adamczyk, Paul Fuierer, Compressive stress in nano-crystalline titanium dioxide films by aerosol deposition, Surf. Coat. Technol. 350 (2018) 542–549.

[20] Jung-Jae Park, Do-Yeon Kim, Jong-Gun Lee, Donghwan Kim, Joon-Ho Oh, Tae-Yeon Seong, Maikel FAM van Hest, Sam S Yoon, Superhydrophilic transparent titania films by supersonic aerosol deposition, J. Am. Ceram. Soc. 96 (5) (2013) 1596–1601.

[21] Matej Sadl, Oana Condurache, Andreja Bencan, Mirela Dragomir, Uros Prah, Barbara Malic, Marco Deluca, Udo Eckstein, Daniel Hausmann, Neamul H Khansur, et al., Energy-storage-efficient 0.9 Pb (Mg1/3Nb2/3) O3–0.1 PbTiO3 thick films integrated directly onto stainless steel, Acta Mater. 221 (2021) 117403.

[22] Chad W Sinclair, Ralf Edinger, Will Sparling, Amin Molavi-Kakhki, Chantal Labrecque, Vibratory powder feeding for powder bed additive manufacturing using water and gas atomized metal powders, Materials 14 (13) (2021) 3548.

[23] Shanyu Wang, Gangjian Tan, Wenjie Xie, Gang Zheng, Han Li, Jihui Yang, Xinfeng Tang, Enhanced thermoelectric properties of Bi 2 (Te 1- x Se x) 3-based compounds as n-type legs for low-temperature power generation, J. Mater. Chem. 22 (39) (2012) 20943–20951.

[24] Hai-Long Yao, Guan-Jun Yang, Chang-Jiu Li, Molecular dynamics simulation and experimental verification for bonding formation of solid-state TiO2 nano-particles induced by high velocity collision, Ceram. Int. 45 (4) (2019) 4700–4706.

[25] Guanyu Song, Huan Yang, Christopher J. Hogan Jr., Thermal energy evolution and mechanical deformation of monocrystalline yttria-stabilized zirconia nanoparticles in aerosol deposition processes, Appl. Surf. Sci. 585 (2022) 152603.

[26] Hesamodin Jami, Ahmad Jabbarzadeh, Unravelling ultrafast deformation mechanisms in surface deposition of titanium nanoparticles, Appl. Surf. Sci. 489 (2019) 446–461.

[27] T.V. Chitrakar, J.W. Keto, M.F. Becker, D. Kovar, Particle deposition and deformation from high speed impaction of Ag nanoparticles, Acta Mater. 135 (2017) 252–262.

[28] Hyunho Kang, Jihyeon Lee, Tana O'Keefe, Beza Tuga, Christopher J Hogan Jr., Christy L Haynes, Effect of (3-aminopropyl) triethoxysilane on dissolution of silica nanoparticles synthesized via reverse micro emulsion, Nanoscale 14 (25) (2022) 9021–9030.

[29] Jihyeon Lee, Siqin He, Guanyu Song, Christopher J Hogan Jr., Size distribution monitoring for chemical mechanical polishing slurries: An intercomparison of electron microscopy, dynamic light scattering, and differential mobility analysis, Powder Technol. 396 (2022) 395–405.

[30] Jesse M Adamczyk, Souvik Ghosh, Tara L Braden, Christopher J Hogan Jr., Eric S Toberer, Alloyed thermoelectric PbTe–SnTe films formed via aerosol deposition, ACS Combin. Sci. 21 (11) (2019) 753–759.

[31] Steve Plimpton, Fast parallel algorithms for short-range molecular dynamics, J. Comput. Phys. 117 (1) (1995) 1–19.

[32] Prabudhya Roy Chowdhury, Jingjing Shi, Tianli Feng, Xiulin Ruan, Prediction of Bi2Te3-Sb2Te3 interfacial conductance and superlattice thermal conductivity using molecular dynamics simulations, ACS Appl. Mater. Interfaces 13 (3) (2021) 4636–4642.

[33] Prabudhya Roy Chowdhury, Tianli Feng, Xiulin Ruan, Development of interatomic potentials for the complex binary compound Sb 2 Te 3 and the prediction of thermal conductivity, Phys. Rev. B 99 (15) (2019) 155202.

[34] Alexander Stukowski, Visualization and analysis of atomistic simulation data with OVITO–the open visualization tool, Modelling Simulation Mater. Sci. Eng. 18 (1) (2009) 015012.

[35] Jiangfeng Ni, Xinyan Li, Menglei Sun, Yifei Yuan, Tongchao Liu, Liang Li, Jun Lu, Durian-inspired design of Bismuth–antimony alloy arrays for robust sodium storage, ACS Nano 14 (7) (2020) 9117–9124.

[36] Ekrem Gunes, Felix Gundlach, Matthias T Elm, Peter J Klar, Sabine Schlecht, Mathias S Wickleder, Eckhard Muller, Nanostructured composites of Bi1–x Sb x nanoparticles and carbon nanotubes and the characterization of their thermoelectric properties, ACS Appl. Mater. Interfaces 9 (51) (2017) 44756–44765.

[37] Jun Akedo, Room temperature impact consolidation (RTIC) of fine ceramic powder by aerosol deposition method and applications to microdevices, J. Therm. Spray Technol. 17 (2) (2008) 181–198.

[38] Michael Schubert, Jörg Exner, Ralf Moos, Influence of carrier gas composition on the stress of Al2O3 coatings prepared by the aerosol deposition method, Materials 7 (8) (2014) 5633–5642.

[39] Jungho Ryu, Kun-Young Kim, Jong-Jin Choi, Byung-Dong Hahn, Woon-Ha Yoon, Byoung-Kuk Lee, Dong-Soo Park, Dae-Yong Jeong, Chan Park, Flexible dielectric Bi1. 5Zn1. 0Nb1. 5o7 thin films on a Cu-polyimide foil, J. Am. Ceram. Soc. 92 (2) (2009) 524–527.

[40] J.E. Blendell, Robert L. Coble, Measurement of stress due to thermal expansion anisotropy in Al2O3, J. Am. Ceram. Soc. 65 (3) (1982) 174–178.

[41] Andreas Leineweber, Thermal expansion anisotropy as source for microstrain broadening of polycrystalline cementite, Fe3C, J. Appl. Crystallogr. 49 (5) (2016) 1632–1644.

[42] Sumit Suresh, Seok-Woo Lee, Mark Aindow, Harold D Brody, Victor K Champagne, Avinash M Dongare, Mesoscale modeling of jet initiation behavior and microstructural evolution during cold spray single particle impact, Acta Mater. 182 (2020) 197–206.

[43] Seongpil An, Bhavana Joshi, Alexander L Yarin, Mark T Swihart, Sam S Yoon, Supersonic cold spraying for energy and environmental applications: One-step scalable coating technology for advanced micro-and nanotextured materials, Adv. Mater. 32 (2) (2020) 1905028.

[44] Kalyan Kottapalli, Harikrishnan Murali, Guanyu Song, Patrick Fillingham, Igor Novosselov, Resuspension of trace explosive particle residues by planar impinging jet: effects of exposure duration and wall shear stress, J. Aerosol Sci. (2022) 106095.

[45] Hossein Aghajani, Zia Valefi, Pejman Zamani, Phase composition, microstructure, mechanical properties, and wear performance of nanostructured Al2O3 and Al2O3-Y2O3 coatings deposited by plasma spraying, Appl. Surf. Sci. 585 (2022) 152754.

[46] Sunghoon Kim, Myung-Yeon Cho, Ik-Soo Kim, Won-Jung Kim, Sung-Han Park, Seungmin Baek, Jong-Min Oh, Sang-Wook Kim, Solvent-free aerosol deposition for highly luminescent and thermally stable Perovskite-ceramic nanocomposite film, Adv. Mater. Interfaces 6 (13) (2019) 1900359.

[47] Mostafa Hassani-Gangaraj, David Veysset, Keith A Nelson, Christopher A Schuh, Melt-driven erosion in microparticle impact, Nature Commun. 9 (1) (2018) 1–7.

[48] Mostafa Hassani-Gangaraj, David Veysset, Keith A Nelson, Christopher A Schuh, Melting can hinder impact-induced adhesion, Phys. Rev. Lett. 119 (17) (2017) 175701.

[49] Gyuyeol Bae, S Kumar, Sanghoon Yoon, Kicheol Kang, Hyuntaek Na, Hyung-Jun Kim, Changhee Lee, Bonding features and associated mechanisms in kinetic sprayed titanium coatings, Acta Mater. 57 (19) (2009) 5654–5666.

[50] Hanqing Che, Andre C Liberati, Xin Chu, Meixin Chen, Amir Nobari, Phuong Vo, Stephen Yue, Metallization of polymers by cold spraying with low melting point powders, Surf. Coat. Technol. 418 (2021) 127229.

[51] Henan Zhou, Doyl E Dickel, Michael I Baskes, Sungkwang Mun, Mohsen Asle Zaeem, A modified embedded-atom method interatomic potential for bismuth, Modelling Simulation Mater. Sci. Eng. 29 (6) (2021) 065008.

[52] Hesamodin Jami, Ahmad Jabbarzadeh, Ultrafast thermomechanical effects in aerosol deposition of hydroxyapatite nanoparticles on a titanium substrate, Surf. Coat. Technol. 382 (2020) 125173.

[53] Daniel Faken, Hannes Jónsson, Systematic analysis of local atomic structure combined with 3D computer graphics, Comput. Mater. Sci. 2 (2) (1994) 279–286.

[54] Aidan H Moyers, Derek W Davies, Michael F Becker, Desiderio Kovar, A molecular dynamics survey study of impact-induced amorphization in yttria nanoparticles, J. Aerosol Sci. 162 (2022) 105976.

[55] Hesamodin Jami, Ahmad Jabbarzadeh, Molecular simulation of high-velocity deposition of titanium dioxide nanoparticles on titanium, Appl. Surf. Sci. 542 (2021) 148567.

[56] M.S. Dresselhaus, Electronic properties of the group V semimetals, J. Phys. Chem. Solids 32 (Suppl 1) (1971) 3–33.

[57] EI Rogacheva, SN Grigorov, ON Nashchekina, S Lyubchenko, MS Dresselhaus, Quantum-size effects in n-type bismuth thin films, Appl. Phys. Lett. 82 (16) (2003) 2628–2630.

[58] B Lenoir, M Cassart, J-P Michenaud, H Scherrer, S Scherrer, Transport properties of Bi-rich Bi-Sb alloys, J. Phys. Chem. Solids 57 (1) (1996) 89–99.

[59] K. Vandaele, M. Otsuka, Y. Hasegawa, J.P. Heremans, Confinement effects, surface effects, and transport in Bi and Bi1- xSbx semiconducting and semimetallic nanowires, J. Phys.: Condens. Matter 30 (40) (2018) 403001.

[60] V.S. Zemskov, A.D. Belaya, U.S. Beluy, G.N. Kozhemyakin, Growth and investigation of thermoelectric properties of Bi–Sb alloy single crystals, J. Cryst. Growth 212 (1–2) (2000) 161–166.

[61] B. Lenoir, H. Scherrer, T. Caillat, An overview of recent developments for BiSb alloys, Semicond. Semimet. 69 (2001) 101–137.